Prediction of superconductivity in pressure-induced new silicon boride phases

Xiaowei Liang [1], Aitor Bergara,[2,3,4] Yu Xie [5,*] Linyan Wang,[1] Rongxin Sun,[1] Yufei Gao,[1] Xiang-Feng Zhou,[1] Bo Xu,[1] Julong He,[1] Dongli Yu,[1] Guoying Gao [1,†] and Yongjun Tian[1]

[1]*Center for High Pressure Science, State Key Laboratory of Metastable Materials Science and Technology, Yanshan University, Qinhuangdao 066004, China*
[2]*Departmento de Física de la Materia Condensada, Universidad del País Vasco, UPV/EHU, 48080 Bilbao, Spain*
[3]*Donostia International Physics Center (DIPC), 20018 Donostia, Spain*
[4]*Centro de Física de Materiales CFM, Centro Mixto CSIC-UPV/EHU, 20018 Donostia, Spain*
[5]*Key Laboratory of Physics and Technology for Advanced Batteries (Ministry of Education) & Innovation Center for Computational Physics Methods and Software & State Key Laboratory of Superhard Materials, College of Physics, Jilin University, Changchun 130012, China*

The crystal structures and properties of boron-silicon (B-Si) compounds under pressure have been systematically explored using particle swarm optimization structure prediction method in combination with first-principles calculations. Three new stoichiometries, B_2Si, BSi, and BSi_2, are predicted to be stable gradually under pressure, where increasing pressure favors the formation of silicon rich B-Si compounds. In the boron-rich compounds, the network of boron atoms changes from B_{12} icosahedron in the ambient phases to the similar buckled graphenelike layers in the high-pressure phases, which crystalize in the same $P\bar{3}m1$ symmetry but with different numbers of boron layers between adjacent silicon layers. Phonon calculations show that these structures might be retained to ambient conditions as metastable phases. Further electron-phonon coupling calculations indicate that the high-pressure phases of boron-rich compounds might superconduct at 1 atm, with the highest T_c value of 21 K from the Allen-Dynes equation in $P\bar{3}m1$ B_2Si, which is much higher than the one observed in boron doped diamond-type silicon. Moreover, further fully anisotropic Migdal-Eliashberg calculations indicate that B_2Si is a two-gap anisotropic superconductor and the estimated T_c might reach up to 30 K at 1 atm. On the silicon-rich side, BSi_2 is predicted to be stable in the $CuAl_2$-type structure. Our current results significantly enrich the phase diagram of the B-Si system and will stimulate further experimental study.

I. INTRODUCTION

Borides have attracted much attention in both fundamental science and industrial applications owing to their potential superconducting, superhard, thermoelectric, and refractory properties [1–12]. These diverse properties are related to a wide variety of structures and boron arrangements in borides (ranging from isolated boron atoms to complex polyhedron) [1–3]. Like most of borides, the known silicon borides consisting of boron polyhedral frameworks have extremely high thermal and chemical stability in high corrosive and high temperature environments, thus they are typically refractory materials and often used in devices operating at extreme conditions [13–15]. Recently, boron-doped silicon has attracted considerable attention for its potential superconductivity [16–19] and its critical superconducting temperature rises up to 0.56 K with increasing the boron content [19].

The B-Si system has been the subject of extensive investigation since 1900 [20]. At ambient pressure and high temperature, three approximate compositions, B_3Si [14,21–23], B_6Si [24,25], and B_nSi ($n \geqslant 14$) [26–28], have been observed in experiments. α-B_3Si, with stoichiometries

ranging from $B_{2.8}Si$ to B_4Si, containing boron-rich icosahedra, was proposed to be rhombohedral, where silicon atoms partially substitute boron atoms in the polar icosahedral sites [22]. This compound forms from direct combination of the elements by isothermal heating at 1225 °C or arc melting in a high-frequency induction furnace. The first fully crystallographically ordered structure, β-B_3Si [14], was produced in Ga flux at a lower temperature (850–1000 °C), and adopts an orthorhombic structure with B atoms forming regular B_{12} icosahedra. Another stoichiometry with an approximate ratio of B:Si = 6:1 (B_6Si) is also known, which contains boron-rich icosahedra, icosihexahedra, as well as isolated silicon and boron atoms. α-B_3Si, β-B_3Si, and B_6Si are all semiconductors with band gaps of 0.2, 2.0, and 1.2 eV, respectively [14,15]. As an extension of solid solution of silicon in boron, the structure of B_nSi ($n \geqslant 14$) is similar to pure β boron [26,27], with silicon atoms partially occupying icosahedral boron atom positions or interstitial sites. It is well known that the physical properties of a material are closely related to its crystal structures. The experimentally observed structures of B_3Si, B_6Si, and B_nSi contain similar B polyhedral frameworks, but there is no report on other structural features formed by B atoms in boron-rich compounds yet. On the silicon-rich side, there is only one theoretical work on BSi_3 by Wang *et al.* [29], where they predicted three metastable structures, $P3_121$, $C2/m$, and $P2_1/m$, in the pressure range of 0–160 GPa,

*xieyu@jlu.edu.cn
†gaoguoying@ysu.edu.cn

which are potential hard materials. Small-size $B_nSi^{0/-}$ clusters and two-dimensional boron-silicon compounds were also theoretically investigated [30–34].

Here, we have extensively investigated the crystal structures and properties of B-Si compounds under pressure by using the particle swarm optimization structure prediction method in combination with first-principles calculations. We first explored the already known B_6Si, B_4Si, and B_3Si stoichiometries and then proceed to the analysis of hypothetical B_2Si, BSi, BSi_2, and BSi_3 stoichiometries. We studied in detail the crystal structures of the preferred compounds as a function of pressure, together with their dynamical stability and corresponding electronic band structures and superconductivity. We found that three new stoichiometries, B_2Si, BSi, and BSi_2, become stable gradually under pressure, where increasing pressure favors the formation of silicon rich B-Si compounds. All the predicted stable high-pressure structures of boron-rich compounds have similar structural characteristics containing buckled graphenelike boron layers. In addition, our calculations indicate that these structures might be preserved to ambient pressure as metastable phases, in which they were predicted to be superconductors with the highest T_c value of 30 K in $P\bar{3}m1$ B_2Si.

II. COMPUTATIONAL DETAILS

Structure searches of B_xSi_y ($x = 2$–4, and 6, $y = 1$; $x = 1$, $y = 1$–3) were performed using the particle swarm optimization method [35,36], as implemented in the CALYPSO code [37]. Such an approach has successfully predicted the high-pressure structures of various systems, ranging from elemental solids to binary and ternary compounds [38–44]. The underlying energetic calculations were performed within the framework of density functional theory (DFT) as implemented in the VASP code [45]. The Perdew-Burke-Ernzerhof generalized gradient approximation was chosen for the exchange-correlation functional [46]. The adopted all-electron projector-augmented wave (PAW) [47] pseudopotentials of B and Si treat $2s^22p^1$ and $3s^23p^2$ electrons as valence electrons, respectively. An energy cutoff of 700 eV and appropriate Monkhorst-Pack k meshes [48] were chosen to ensure that enthalpy calculations were well converged within 1 meV/f.u. Phonon calculations were performed by the direct supercell method [49] or density functional perturbation theory (DFPT) with the PHONOPY [50] and QUANTUM-ESPRESSO codes [51], respectively. Electron-phonon coupling (EPC) calculations use the ultrasoft pseudopotential method within DFPT. Convergence tests concluded a kinetic energy cutoff of 60 Ry. $6 \times 6 \times 6$, $8 \times 8 \times 6$, $9 \times 9 \times 3$, and $7 \times 7 \times 4$ q-point meshes in the first Brillouin zone were used in the EPC calculation for $R\bar{3}m$ B_2Si, $P\bar{3}m1$ B_2Si, $P\bar{3}m1$ B_3Si, and $P\bar{3}m1$ B_4Si, respectively. Correspondingly, Monkrost-Pack grids of $24 \times 24 \times 24$, $32 \times 32 \times 24$, $36 \times 36 \times 12$, and $28 \times 28 \times 16$ were used to ensure k-point sampling convergence with Gaussians of width 0.02 Ry. The superconducting gap of $P\bar{3}m1$ B_2Si was estimated using the anisotropic Migdal-Eliashberg formalism [52,53] as implemented in the EPW code [54–56]. We used norm-conserving pseudopotentials with a plane-wave basis up to 60 Ry. The electron-phonon

matrix elements were calculated on coarse phonon and electron grids of $7 \times 7 \times 5$ and $14 \times 14 \times 10$, respectively, and then interpolated onto fine q and k grids of $56 \times 56 \times 40$ and $56 \times 56 \times 40$ by Wannier-Fourier interpolation [57,58].

III. RESULTS AND DISCUSSION

The crystal structure searches of B_xSi_y ($x = 2$–4, and 6, $y = 1$; $x = 1$, $y = 1$–3) were carried out with system sizes containing up to 8 formula units (f.u.) per simulation cell over a wide pressure range of 0–400 GPa. Our structure prediction starts from the already known compounds at low pressure. For B_3Si, an orthorhombic $Pmma$ structure was predicted to be stable against decomposition into elements (B and Si). Its structure is very similar to the experimentally observed $Imma$ β-B_3Si (Fig. S1 [59]). Both structures are composed of interlinked B_{12} cages and Si_4 chains. However, there is a little difference in the relative positions of some Si atoms (atoms 2 and 4) [Fig. S1(a) [59]]. We made an estimation of the energy barrier between them by shifting Si atoms and the calculated maximum energy barrier reaches 0.12 eV/f.u. at 0 K [Fig. S1(b) [59]], which prevents the transition from $Pmma$ to $Imma$. However, this barrier can be easily overcome at high temperatures so that the two structures might be interchangeable.

For B_4Si and B_6Si, a series of energetically competitive structures (Figs. S2-3 [59]) were predicted to contain B-rich cages, in agreement with the experimental observations. The predicted $R\bar{3}m$ B_6Si is isomorphous with the well-known $R\bar{3}m$ B_6O [60]. $Cmcm$ B_6Si is the most stable phase between 0 and 17.5 GPa and then transforms to a similar $Cmca$ structure, which is the same with the $Cmca$ LiB_6Si getting rid of Li atoms [61]. Different from B_3Si, all the predicted structures for B_4Si and B_6Si are metastable with positive formation enthalpies, though the enthalpies of $P2/c$ B_4Si are only 3–11 meV higher than those of 4B+Si at the pressure range of 0–10 GPa. Notably, all the already known B-Si compounds, with the exception of β-B_3Si, were observed to be disordered and the prediction of disordered structures goes beyond the scope of our research. However, the successful prediction of β-B_3Si and B_4Si and B_6Si cagelike structures confirms the reliability of our method.

To explore the possible new stoichiometries, we focused our structural searches on B_xSi_y at 1 atm, 10, 50, 100, 200, 300, and 400 GPa. The thermodynamic stabilities were evaluated by calculating their formation enthalpies relative to the products of dissociation into constituent elements. As references, the $R\bar{3}m$, $Pnnm$, $Cmca$, and $P6_3/mcm$ structures for B and $Fd\bar{3}m$, $P6_3/mcm$, and $Fm\bar{3}m$ for Si are considered, each in its most stable form at the specified pressure [62–64]. To account for the enthalpy relationships of each stoichiometry, a convex hull for the B-Si system was calculated at different pressures, as depicted in Fig. 1(a). Formation enthalpies of compounds are located on the hull, showing they are thermodynamically stable with respect to elements or other binary compounds. At 50 GPa, the already known B-rich compounds are predicted to decompose into elemental B and Si, and no other stoichiometries can be formed. With increasing pressure to 65 GPa, B_2Si, B_3Si, and B_4Si become energetically favored over elemental
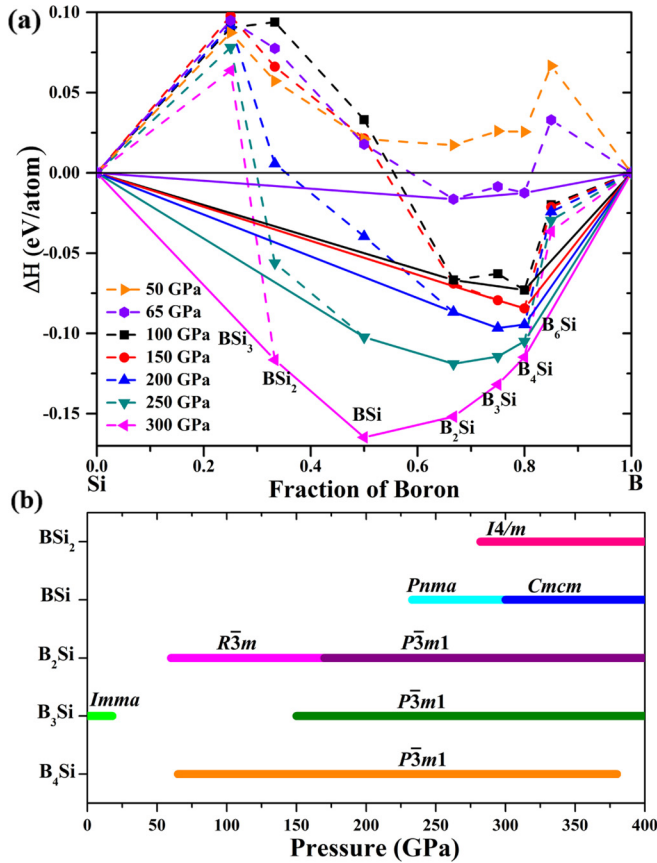
FIG. 1. (a) Formation enthalpies (ΔH) per atom of the $B_x Si_y$ phases with respect to their separated counterparts at 50–300 GPa. The symbols located on the solid lines indicate that the compound is stable at the corresponding pressure. (b) The predicted pressure-composition phase diagram of the B-Si system.

FIG. 2. Predicted stable crystal structures of studied B-Si compounds under pressure. (a) $Pnma$ BSi at 250 GPa. (b) $Cmcm$ BSi at 350 GPa. (c) $P\bar{3}m1$ B_2Si at 200 GPa. (d) $R\bar{3}m$ B_2Si at 100 GPa. (e) $P\bar{3}m1$ B_3Si at 150 GPa. (f) $P\bar{3}m1$ B_4Si at 100 GPa. (g) $I4/m$ BSi_2 at 300 GPa. Blue and orange spheres represent B and Si atoms, respectively.

dissociation, although B_3Si is still unstable against decomposition into B_2Si and B_4Si. As pressure increases to 150 GPa, the formation enthalpies of B_2Si, B_3Si, and B_4Si become more and more negative (more stable) and eventually B_3Si falls on the convex hull. Upon further compression, at 250 and 300 GPa, BSi and BSi_2, respectively, gradually become stable with respect to disproportionation into other stoichiometries. Pressure clearly favors the formation of B-Si compounds with a high content of silicon. Interestingly, as pressure increases from 65 to 250 GPa, B_2Si becomes easier to form. Similarly, pressure also plays a positive role in the formation of BSi.

The predicted pressure-composition phase diagram and respective enthalpy curves of corresponding B-Si compounds are shown in Fig. 1(b) and Fig. S4 [59], respectively. An orthorhombic $Pnma$ BSi is predicted to be stable between 233 and 300 GPa and transforms into an energetically favored $Cmcm$ structure above 300 GPa. $R\bar{3}m$ and $P\bar{3}m1$ B_2Si are enthalpically stable at pressure ranges of 60–170 GPa and 170–400 GPa, respectively. The experimentally observed β-B_3Si and the similar theoretically predicted $Pmma$ structure are stable up to 18 GPa. Note that B_3Si decomposes into pure elements and other compounds at the pressure range of 18–150 GPa, while it becomes stable again with a $P\bar{3}m1$ structure above 150 GPa. The $P\bar{3}m1$ structure for B_4Si is
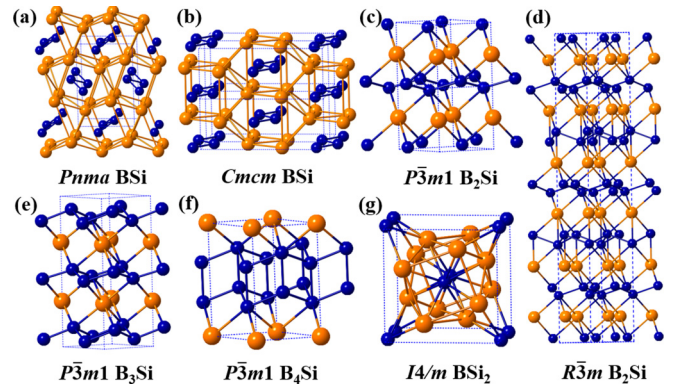
stable over a wide pressure range of 65–380 GPa and $I4/m$ BSi_2 will be stable at pressures between 282 and 400 GPa.

As a basic requirement for the structural stability, the dynamical stability of various structures for B-Si compounds is also examined. The phonon dispersion curves of all the predicted structures in the corresponding stable pressure ranges are presented in Fig. S13 [59]. The absence of any imaginary phonon frequency in the entire Brillouin zone shows they are dynamically stable. Interestingly, $R\bar{3}m$ and $P\bar{3}m1$ B_2Si, $C2/m$ and $P\bar{3}m1$ B_3Si, and $P\bar{3}m1$ B_4Si were also calculated to be dynamically stable at 1 atm, which indicates that these predicted high-pressure phases might be also retained to ambient pressure.

The predicted stable structures are shown in Fig. 2. Both $Pnma$ and $Cmcm$ structures of BSi are orthorhombic and have the same configurations as the already known $Pnma$ FeB and $Cmcm$ CrB, respectively [2]. In both structures, B atoms form zigzag chains and Si atoms form a column of trigonal prisms arranging along the B-B chains. With increasing B content, the B-B bonding changes significantly. As shown in Figs. 2(c) and 2(d), the zigzag B-B chains in BSi transform to buckled six-membered rings in the predicted structures for B_2Si. The $P\bar{3}m1$ B_2Si is similar to the structure of MgB_2. Si atoms are located at edges of the unit cell and a deformed graphenelike boron layer is located between Si layers. The $R\bar{3}m$ B_2Si can be considered a slight modification of the $P\bar{3}m1$ structure, containing two types of boron atoms with coordination numbers of 6 and 7, respectively. Interestingly, the predicted stable high-pressure structures of B_3Si and B_4Si have similar geometries to that of B_2Si, which are crystalized in the same $P\bar{3}m1$ symmetry. For $P\bar{3}m1$ B_3Si and B_4Si, B atoms also exist in the form of buckled graphenelike layers [65]. The main difference between $P\bar{3}m1$ B_2Si, B_3Si, and B_4Si is the number of boron layers between adjacent silicon layers, which increases with increasing the boron content. However, as boron content increases to B_6Si, where the predicted structures present more than three boron layers between silicon layers (Fig. S5 [59]), it is unstable over the whole studied pressure range with respect to decomposing into B_4Si and B [Fig. S4(e) [59]]. In addition,

some metastable structures of BSi, B_2Si, B_3Si, and B_4Si are also shown in Fig. S6 [59], which also presents similar structural characteristics to the predicted stable high-pressure structures.

For Si-rich compounds, the predicted $I4/m$ BSi_2 [Fig. 2(g)] is similar to the well-known $CuAl_2$-type arrangement (some semi-transition-metal borides such as Ti_2B, Ta_2B, and Mo_2B also show the $I4/m$ symmetry [66]), in which B atoms form linear chains, where each B is surrounded by eight Si atoms. BSi_3 was calculated to be unstable and dissociates into pure elements even at 400 GPa. The predicted P-1 and $P2_1/m$-2 phases of BSi_3 (Fig. S7 [59]) are energetically more stable than the $C2/m$ phase predicted by Wang *et al.* [29] in the corresponding pressure range.

The electron localization functions (ELFs) were calculated in order to understand the nature of the chemical bonds. As illustrated in Fig. S8 [59], high ELF values are distributed between B atoms as well as between B and Si atoms, indicating the presence of B-B and B-Si covalent bonds. In both $R\bar{3}m$ and $P\bar{3}m1$ B_2Si, all B atoms are bonded to Si atoms. However, in the $P\bar{3}m1$ B_3Si and B_4Si, with multiboron layers, those B atoms further located away from Si atoms are only bonded to other B atoms. Bader charge calculations [67] have also been performed to analyze the charge transfer between atoms (Table S1 [59]). At 1 atm, each Si atom transfers 1.56 and 1.2 electrons to two B atoms in $R\bar{3}m$ and $P\bar{3}m1$ B_2Si, respectively. With increasing B content, in B_3Si and B_4Si, there are still only two B atoms accepting electrons from one Si atom; the remaining B atoms even act as electron donors, transferring electrons to the two B atoms bonded to the Si atom. These results are consistent with the ELF calculations presented above.

The calculated electronic band structures and density of states (DOS) of stable structures of B-rich compounds are shown in Fig. 3 and Fig. S9 [59]. Several bands crossing the Fermi level (E_f) reveal the metallic character of these structures at 1 atm. Similar to MgB_2, the B p orbits give main contributions to the electronic states near the E_f. Band projections onto B p_x, p_y, and p_z orbitals are also shown in the band structures of $P\bar{3}m1$ B_2Si, B_3Si, and B_4Si. In $P\bar{3}m1$ B_2Si [Fig. 3(a)], the flat bands along the Γ-A direction and around Γ point near the E_f are mainly derived from B $p_{x,y}$, while the steep bands crossing E_f derived from B p_z. Moreover, along the Γ-A direction the nearly cylindrical Fermi surfaces also appeared, which arise from $p_{x,y}$ B bands (Fig. S10 [59]). These characters in $P\bar{3}m1$ B_2Si are similar to those in MgB_2 [68], which might imply the superconductivity of $P\bar{3}m1$ B_2Si. On the other hand, the flat bands close to the E_f corresponding to localized electronic states lead to a large DOS value at E_f, which might also favor an enhancement of the electron-phonon interaction. As we mentioned earlier, B atoms exist in the forms of wrinkled single and double layers in $P\bar{3}m1$ B_2Si and B_4Si, respectively, while both forms of B atoms are alternately arranged in $P\bar{3}m1$ B_3Si. Thus the band structure of $P\bar{3}m1$ B_3Si [Fig. 3(c)] has similar characteristics to that of $P\bar{3}m1$ B_2Si [Fig. 3(a)] and B_4Si [Fig. 3(e)], respectively. Along the Γ-A line and around Γ point in the band structure of $P\bar{3}m1$ B_3Si, the B $p_{x,y}$ dominated bands near E_f are mainly related to the single-layer B atoms, while the bands around 2 and -2 eV are relevant to the double-layer B atoms.
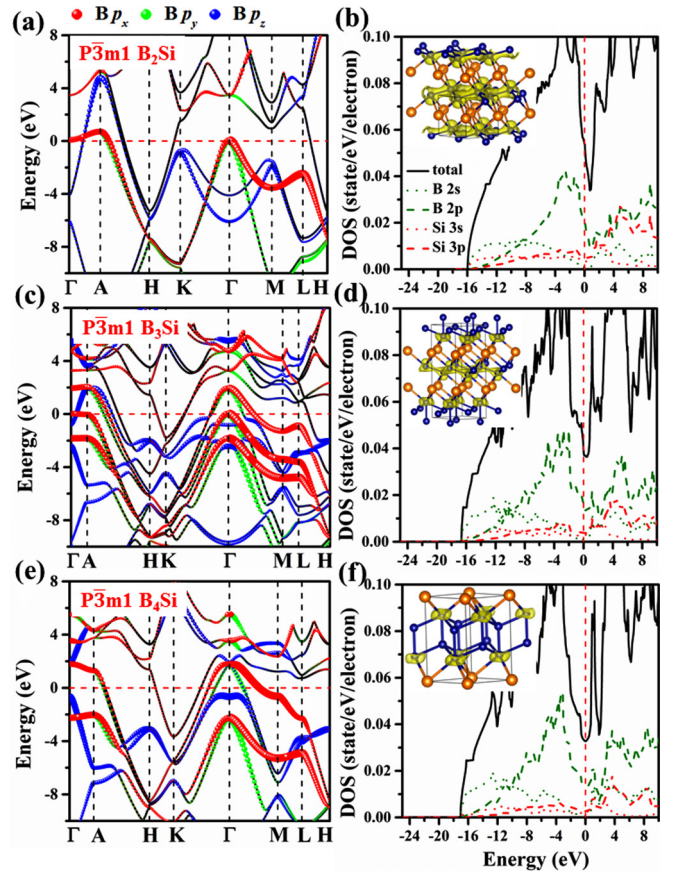

FIG. 3. Calculated electronic band structures and density of states for (a), (b) $P\bar{3}m1$ B_2Si, (c), (d) $P\bar{3}m1$ B_3Si, and (e), (f) $P\bar{3}m1$ B_4Si at 1 atm. The bands projected onto B p_x, p_y and p_z orbitals are displayed in the band structures (the radii of the circles are proportional to the weights of the corresponding orbitals). The insets in (b), (d), and (f) show the distributions of partial charge density with isosurface of 0.018 for states around the Fermi level.

Moreover, $P\bar{3}m1$ B_2Si shows the highest DOS at Fermi level, while the lowest one corresponds to $P\bar{3}m1$ B_4Si. From B_2Si to B_4Si the position of the Fermi level gradually slides down to the valley of the pseudogap.

The insets in the right panels of Fig. 3 show the calculated partial charge densities with isosurface of 0.018 of states around the Fermi level. It can be seen that the calculated charge densities are mainly distributed around B atoms. In $P\bar{3}m1$ B_2Si, B-B σ-bond orbitals form conducting channels for valence electrons. Charge densities of states around the Fermi level come from connected electronic channels in the graphenelike B layer. With increasing the number of B layers in B_3Si and B_4Si, the electronic channels are gradually destroyed, and charge densities are mainly distributed around the B atoms bonded with Si atoms, which suggests the charge transfer from Si to B atoms. Moreover, the other B atoms that are not bonded with Si atoms lose electrons and act as donors. According to the calculated partial charge densities, the metallicity of $P\bar{3}m1$ B_2Si is stronger than that of $P\bar{3}m1$ B_3Si and B_4Si, which is consistent with the calculated DOS. Additionally, the electronic properties of
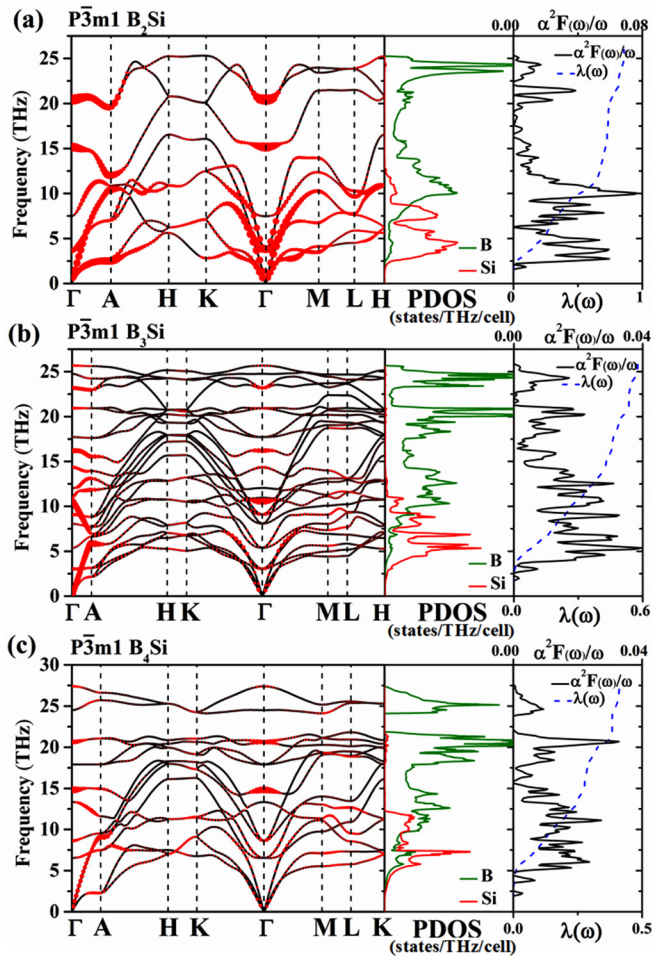
FIG. 4. Calculated phonon dispersion curves (the area of the red circles is proportional to the electron-phonon coupling strength), projected phonon density of states (PDOS), the Eliashberg phonon spectral function $\alpha^2 F(\omega)/\omega$ and the electron-phonon integral $\lambda(\omega)$ of (a) $P\bar{3}m1$ B_2Si, (b) $P\bar{3}m1$ B_3Si, and (c) $P\bar{3}m1$ B_4Si at 1 atm.

FIG. 5. Estimated T_c values of similar structures $P\bar{3}m1$ B_2Si, $P\bar{3}m1$ B_3Si, and $P\bar{3}m1$ B_4Si at 1 atm. The inset shows the evolution of the corresponding electron-phonon coupling parameter λ and logarithmic average frequency ω_{log} with increasing the B content from B_2Si to B_4Si.

the predicted low-pressure structures of B-rich compounds and high-pressure structures of BSi and BSi_2 are shown in Fig. S11 [59]. β-B_3Si was estimated to be a semiconductor with an indirect band gap of about 1.3 eV, which is consistent with previous study [14]. The high-pressure phases of BSi and BSi_2 are metallic.

As mentioned above, the predicted high-pressure structures of B-rich compounds are metastable at 1 atm, with structural characteristics similar to MgB_2. Having in mind that MgB_2 is a good superconductor, with a T_c of 39 K, we thus performed phonon dispersion, projected phonon DOS, Eliashberg spectral function $\alpha^2 F(\omega)/\omega$, and its integral $\lambda(\omega)$ to further explore the superconducting properties of the predicted metallic phases of B_2Si, B_3Si, and B_4Si at 1 atm (Fig. 4). For B_2Si, the calculated phonon DOS can be separated into two regions. The low-frequency vibrations (0–12.5 THz) are associated with both Si and B atoms and high-frequency modes are only related to B atoms. The calculated logarithmic average frequency ω_{log} is 393 K and the EPC parameter λ is 0.86. The main contribution to the EPC comes from the low-
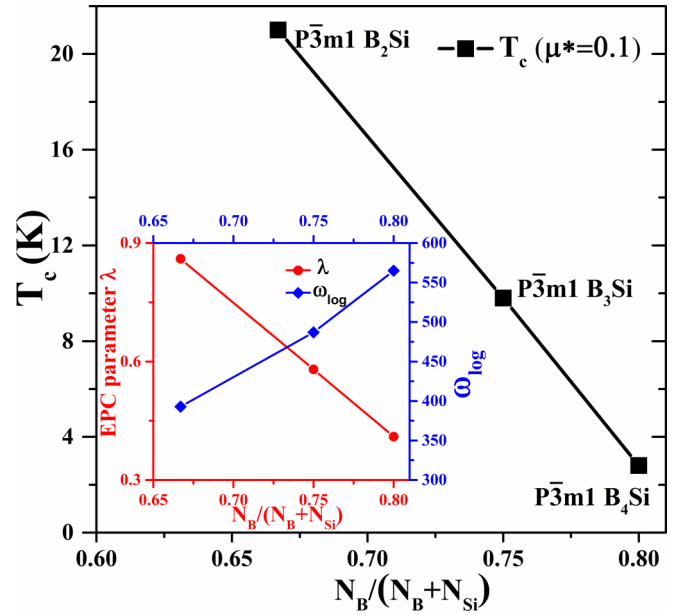
frequency modes, with 78% of the total λ. To further explore the contribution of different phonon modes, red circles with the area proportional to the EPC strength are also plotted in the phonon dispersion curves. All the phonon modes along Γ-A direction have large contributions to the EPC, as well as the soft modes around Γ point. The cases in $P\bar{3}m1$ B_3Si and B_4Si are similar to that of B_2Si. However, the calculated EPC parameter λ decreases from 0.86 in $P\bar{3}m1$ B_2Si to 0.68 and 0.41 in $P\bar{3}m1$ B_3Si and B_4Si, respectively (Fig. 5), which mainly comes from the decreased contribution of the low-frequency modes from 78%, 69% to 56%, respectively.

The T_c values of these predicted phases were calculated by using the Allen-Dynes modified McMillan equation [69]. As shown in Fig. 5, the estimated T_c of $P\bar{3}m1$ B_2Si, B_3Si, and B_4Si at 1 atm is 21–17.5, 9.8–6.8, and 2.8–1.3 K by applying a Coulomb pseudopotential μ^* of 0.1–0.13, respectively, where T_c decreases with increasing B content. The trends of ω_{log} and λ as a function of the B content are shown in the inset of Fig. 5. The calculated ω_{log} increases with increasing B content, which can be attributed to the presence of more and stronger B-B bonds. However, λ presents an opposite evolution to ω_{log}. In addition, $R\bar{3}m$ B_2Si and $Pnma$ BSi are also estimated to superconduct with T_c of 7.7 and 2.4 K at 1 atm and 250 GPa, respectively (Fig. S12 [59]). Our results show that most of the predicted high-pressure phases of B-Si compounds are potential superconductors. $P\bar{3}m1$ B_2Si shows the highest T_c value of 21 K at 1 atm, which is much higher than the experimentally observed T_c of 0.56 K [19] in boron doped diamond-type silicon.

As we know, MgB_2 is a prototypical anisotropic superconductor. Considering the similarity between B_2Si and MgB_2,
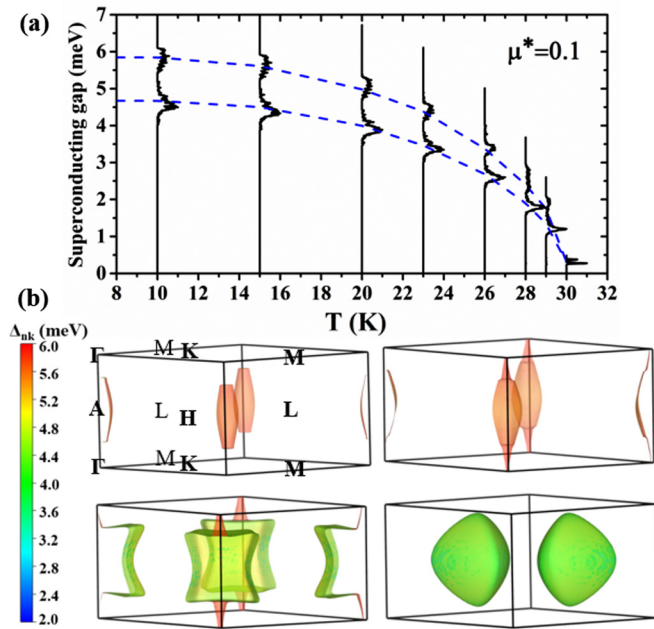
FIG. 6. (a) Calculated anisotropic superconducting gap of $P\bar{3}m1$ B_2Si at 1 atm on the Fermi surface as a function of temperature. (b) The superconducting energy gap of B_2Si, calculated at 10 K, mapped on the four Fermi surface sheets.

the superconducting anisotropy of $P\bar{3}m1$ B_2Si was also investigated by combining the fully anisotropic Migdal-Eliashberg theory [52,53] with the electron-phonon interpolation based on maximally localized Wannier functions [57]. Figure 6(a) shows the calculated superconducting energy gap Δ_{nk} as a function of temperature with μ^* of 0.1. One can clearly see that the $P\bar{3}m1$ B_2Si displays an anisotropic superconductivity with a two-gap nature. From the momentum-resolved superconducting gap Δ_{nk} on the Fermi surface at 10 K [Fig. 6(b)], we find that the higher Δ_{nk} values are distributed on the two Fermi surface sheets along the Γ-A-Γ line associated to the $p_{x,y}$ orbitals of boron, while the lower Δ_{nk} values are mapped on the remaining Fermi surface sheets. In comparison, the energy difference of 1.2 meV between two average Δ_{nk} values in B_2Si is much smaller than that of 6.5 meV in MgB_2 at 10 K [56], indicating that B_2Si is less anisotropic. In MgB_2, there are not only strong covalent B-B bonds in the graphenelike planes, but also ionic bonds between Mg and B atoms. Two degenerate σ-bond bands associated to B atoms are highly coupled with the E_{2g} phonon mode, which is mainly associated with the B atomic motion [70]. However, in the predicted B_2Si, the interplane B-Si bonds are also strongly covalent. The bands near the Fermi level mainly associated to B orbitals are not only coupled with B-related phonon modes, but also with Si-related ones. As temperature increases, the superconducting gap will decrease. The critical temperature

T_c can be estimated when the superconducting gap value vanishes. As shown in Fig. 6(a), the critical temperature T_c for $P\bar{3}m1$ B_2Si is 30 K, which is higher than that of 21 K derived with the Allen-Dynes formula.

IV. CONCLUSIONS

In summary, we have systematically explored the crystal structures and novel properties of B-Si compounds under pressure. At 1 atm, we reproduced the experimentally observed ordered structure β-B_3Si and also successfully predicted a series of structures containing B_{12} units for B_6Si and B_4Si, which are similar to the experimental ones. Upon compression, new compositions, B_2Si, BSi, and BSi_2, become gradually stable, indicating that pressure promotes the formation of B-Si compounds with high silicon content. On the B-rich side, from B_2Si to B_6Si, all the predicted stable high-pressure structures contain buckled graphenelike boron layers and the number of boron layers between adjacent silicon layers increases with increasing the boron content. Phonon calculations show these structures are dynamically stable, so that they might be preserved as metastable phases at 1 atm. Electronic band structure calculations show that all the stable high-pressure phases are metallic. Moreover, electron-phonon coupling calculations indicate that all the retained high-pressure phases of B-rich compounds are superconductors at 1 atm. $P\bar{3}m1$ B_2Si has the highest T_c value of 21 K at 1 atm, which is much higher than that of the observed one in B doped diamond-type Si. Within the fully anisotropic Migdal-Eliashberg formalism, our calculations suggest that $P\bar{3}m1$ B_2Si is a two-gap anisotropic superconductor and the estimated T_c might reach up to 30 K at 1 atm. Our studies not only enrich the phase diagram of the B-Si system but also may stimulate experimental exploration of superconductivity in B-Si compounds. Moreover, the B-Si system will be helpful for further understanding structural and physical properties of boron-rich compounds under pressure.

[1] B. Albert and H. Hillebrecht, Angew. Chem. Int. Ed. **48**, 8640 (2009).

[2] G. Akopov, M. T. Yeung, and R. B. Kaner, Adv. Mater. **29**, 1604506 (2017).

[3] A. V. D. Geest and A. Kolmogorov, Calphad **46**, 184 (2014).

[4] J. Nagamatsu, N. Nakagawa, T. Muranaka, Y. Zenitani, and J. Akimitsu, Nature (London) **410**, 63 (2001).

[5] H. Gou, N. Dubrovinskaia, E. Bykova, A. A. Tsirlin, D. Kasinathan, W. Schnelle, A. Richter, M. Merlini, M. Hanfland, A. M. Abakumov *et al.*, Phys. Rev. Lett. **111**, 157002 (2013).

[6] H. Rosner, A. Kitaigorodsky, and W. E. Pickett, Phys. Rev. Lett. **88**, 127001 (2002).

[7] A. N. Kolmogorov, S. Shah, E. R. Margine, A. F. Bialon, T. Hammerschmidt, and R. Drautz, Phys. Rev. Lett. **105**, 217003 (2010).

[8] H.-Y. Chung, M. B. Weinberger, J. B. Levine, A. Kavner, J.-M. Yang, S. H. Tolbert, and R. B. Kaner, Science **316**, 436 (2007).

[9] M. Mukaida, T. Goto, and T. Hirai, Mater. Manuf. Process. **7**, 625 (1992).

[10] B. Armas, C. Combescure, J. Dusseau, T. Lepetre, J. Robert, and B. Pistoulet, J. Less Common Met. **47**, 135 (1976).

[11] C. Wood, Rep. Prog. Phys. **51**, 459 (1988).

[12] T. Lundstrom, Pure Appl. Chem. **57**, 1383 (1985).

[13] H. Rizzo, B. Weber, and M. Schwartz, J. Am. Ceram. Soc. **43**, 497 (1960).

[14] J. R. Salvador, D. Bilc, S. Mahanti, and M. G. Kanatzidis, Angew. Chem. Int. Ed. **42**, 1929 (2003).

[15] Y. Imai, M. Mukaida, M. Ueda, and A. Watanabe, J. Alloy Compd. **347**, 244 (2002).

[16] E. Bustarret, C. Marcenat, P. Achatz, J. Kačmarčik, F. Lévy, A. Huxley, L. Ortéga, E. Bourgeois, X. Blase, D. Débarre *et al.*, Nature (London) **444**, 465 (2006).

[17] K. Kádas, L. Vitos, and R. Ahuja, Appl. Phys. Lett. **92**, 052505 (2008).

[18] X. Blase, E. Bustarret, C. Chapelier, T. Klein, and C. Marcenat, Nat. Mater. **8**, 375 (2009).

[19] C. Marcenat, J. Kačmarčík, R. Piquerel, P. Achatz, G. Prudon, C. Dubois, B. Gautier, J. C. Dupuy, E. Bustarret, L. Ortega, T. Klein, J. Boulmer, T. Kociniewski, and D. Debarre, Phys. Rev. B **81**, 020501(R) (2010).

[20] H. Moissan and A. Stock, C. R. Acad. Sci. (Paris) **131**, 139 (1900).

[21] R. Olesinski and G. Abbaschian, Bull. Alloy Phase Diagr. **5**, 478 (1984).

[22] B. Magnusson and C. Brosset, Acta Chem. Scand. **16**, 449 (1962).

[23] T. Aselage, J. Mater. Res. **13**, 1786 (1998).

[24] R. Adamsky, Acta Crystallogr. **11**, 744 (1958).

[25] C. F. Cline, J. Electrochem. Soc. **106**, 322 (1959).

[26] R. Geise, Jr., J. Economy, and V. Matkovich, Z. Kristallogr. **122**, 144 (1965).

[27] M. Vlasse and J. Viala, J. Solid State Chem. **37**, 181 (1981).

[28] J. Viala and J. Bouix, J. Less Common Met. **71**, 195 (1980).

[29] J. Wang, G. Sun, P. Kong, W. Sun, C. Lu, F. Peng, and X. Kuang, Phys. Chem. Chem. Phys. **19**, 16206 (2017).

[30] D. T. T. Mai, L. V. Duong, T. B. Tai, and M. T. Nguyen, J. Phys. Chem. A **120**, 3623 (2016).

[31] T. B. Tai, P. Kadłubański, S. Roszak, D. Majumdar, J. Leszczynski, and M. T. Nguyen, Chem. Phys. Chem. **12**, 2948 (2011).

[32] X. Tan, F. Li, and Z. Chen, J. Phys. Chem. C **118**, 25825 (2014).

[33] X. Tan, C. R. Cabrera, and Z. Chen, J. Phys. Chem. C **118**, 25836 (2014).

[34] Y. Ding and Y. Wang, J. Phys. Chem. C **117**, 18266 (2013).

[35] Y. Wang, J. Lv, L. Zhu, and Y. Ma, Phys. Rev. B **82**, 094116 (2010).

[36] J. Lv, Y. Wang, L. Zhu, and Y. Ma, J. Chem. Phys. **137**, 084104 (2012).

[37] Y. Wang, J. Lv, L. Zhu, and Y. Ma, Comput. Phys. Commun. **183**, 2063 (2012).

[38] L. Zhu, H. Liu, C. J. Pickard, G. Zou, and Y. Ma, Nat. Chem. **6**, 644 (2014).

[39] X. Liang, A. Bergara, L. Wang, B. Wen, Z. Zhao, X.-F. Zhou, J. He, G. Gao, and Y. Tian, Phys. Rev. B **99**, 100505(R) (2019).

[40] L. Wang, F. Tian, X. Liang, Y. Fu, X. Mu, J. Sun, X.-F. Zhou, K. Luo, Y. Zhang, Z. Zhao *et al.*, Phys. Rev. B **99**, 174104 (2019).

[41] L. Zhu, H. Wang, Y. Wang, J. Lv, Y. Ma, Q. Cui, Y. Ma, and G. Zou, Phys. Rev. Lett. **106**, 145501 (2011).

[42] J. Lv, Y. Wang, L. Zhu, and Y. Ma, Phys. Rev. Lett. **106**, 015503 (2011).

[43] J. Lin, S. Zhang, W. Guan, G. Yang, and Y. Ma, J. Am. Chem. Soc. **140**, 9545 (2018).

[44] Z. Zhao, S. Zhang, T. Yu, H. Xu, A. Bergara, and G. Yang, Phys. Rev. Lett. **122**, 097002 (2019).

[45] G. Kresse and J. Furthmüller, Phy. Rev. B **54**, 11169 (1996).

[46] J. P. Perdew, K. Burke, and M. Ernzerhof, Phys. Rev. Lett. **77**, 3865 (1996).

[47] P. E. Blöchl, Phys. Rev. B **50**, 17953 (1994).

[48] H. J. Monkhorst and J. D. Pack, Phys. Rev. B **13**, 5188 (1976).

[49] K. Parlinski, Z. Q. Li, and Y. Kawazoe, Phys. Rev. Lett. **78**, 4063 (1997).

[50] A. Togo, F. Oba, and I. Tanaka, Phys. Rev. B **78**, 134106 (2008).

[51] P. Giannozzi, S. Baroni, N. Bonini, M. Calandra, R. Car, C. Cavazzoni, D. Ceresoli, G. L. Chiarotti, M. Cococcioni, I. Dabo *et al.*, J. Phys.: Condens. Matter **21**, 395502 (2009).

[52] P. B. Allen and B. Mitrović, *Solid State Physics* (Elsevier, Amsterdam, 1983), Vol. 37, pp. 1–92.

[53] E. R. Margine and F. Giustino, Phys. Rev. B **87**, 024505 (2013).

[54] F. Giustino, M. L. Cohen, and S. G. Louie, Phys. Rev. B **76**, 165108 (2007).

[55] J. Noffsinger, F. Giustino, B. D. Malone, C.-H. Park, S. G. Louie, and M. L. Cohen, Comput. Phys. Commun. **181**, 2140 (2010).

[56] S. Poncé, E. R. Margine, C. Verdi, and F. Giustino, Comput. Phys. Commun. **209**, 116 (2016).

[57] N. Marzari, A. A. Mostofi, J. R. Yates, I. Souza, and D. Vanderbilt, Rev. Mod. Phys. **84**, 1419 (2012).

[58] A. A. Mostofi, J. R. Yates, Y.-S. Lee, I. Souza, D. Vanderbilt, and N. Marzari, Comput. Phys. Commun. **178**, 685 (2008).

[59] See Supplemental Material at http://link.aps.org/supplemental/10.1103/PhysRevB.101.014112 for the structural comparison and energy barrier between β-B_3Si (*Imma*) and predicted *Pmma*B_3Si at 1 atm; the predicted metastable structures for B_4Si and B_6Si at 1 atm; the calculated enthalpy curves for different B-Si compounds as a function of pressure, with respect to the elements and other stoichiometries; the predicted metastable

structures for B-Si compounds under pressure; the calculated ELFs and band structures of some predicted stable structures of B-Si compounds; the calculated band structure and DOS for $R\bar{3}m$B$_2$Si at 1 atm; the Fermi surface of $P\bar{3}m$1 B$_2$Si at 1 atm; the superconductivity for $R\bar{3}m$B$_2$Si and *Pnma* BSi at 1 atm and 250 GPa, respectively; phonon spectra of the various structures; the Bader charge analysis for predicted stable B-rich phases at 1 atm; the calculated T_c for various predicted stable phases at different pressures; detail structural information of predicted B-Si compounds at selected pressures.

[60] I. Higashi, M. Kobayashi, J. Bernhard, C. Brodhag, and F. Thévenot, AIP Conf. Proc. **231**, 201 (1991).

[61] N. Vojteer, M. Schroeder, C. Roehr, and H. Hillebrecht, Chem. Eur. J. **14**, 7331 (2008).

[62] Y. Yao and D. D. Klug, Phys. Rev. B **85**, 214122 (2012).

[63] A. R. Oganov, J. Chen, C. Gatti, Y. Ma, Y. Ma, C. W. Glass, Z. Liu, T. Yu, O. O. Kurakevych, and V. L. Solozhenko, Nature (London) **457**, 863 (2009).

[64] D. Li, K. Bao, F. Tian, X. Jin, D. Duan, Z. He, B. Liu, and T. Cui, RSC Adv. **4**, 203 (2014).

[65] J. Kunstmann and A. Quandt, Phys. Rev. B **74**, 035413 (2006).

[66] M. Wang, C. Liu, M. Wen, Q. Li, and Y. Ma, Phys. Chem. Chem. Phys. **19**, 31592 (2017).

[67] R. Bader, *Atoms in Molecules: A Quantum Theory* (Oxford University Press, Oxford, 1994).

[68] J. Kortus, I. I. Mazin, K. D. Belashchenko, V. P. Antropov, and L. L. Boyer, Phys. Rev. Lett. **86**, 4656 (2001).

[69] P. B. Allen and R. Dynes, Phys. Rev. B **12**, 905 (1975).

[70] Y. Kong, O. V. Dolgov, O. Jepsen, and O. K. Andersen, Phys. Rev. B **64**, 020501(R) (2001).